RSC Advances

PAPER

View Article Online
View Journal | View Issue

Cite this: *RSC Adv.*, 2020, **10**, 8618

The tesseract in two dimensional materials, a DFT approach†

Long Zhou,[a] Guanglong Zhang,[a] Fangyuan Xiu,[b] Shuwei Xia *[a] and Liangmin Yu[a]

A series of novel two-dimensional materials inspired from a 4D polytope, tesseract, have been proposed by density functional theory (DFT) based computations. Both $C_{24}X_{12}$ and $C_{16}X_{16}$ (X = O, S and Se) are found to have great thermodynamic and dynamic stabilities, and $C_{24}X_{12}$ exhibited excellent thermal stability up to 1000 K. All these 2D crystals are semiconductors with 2.17 eV to 3.35 eV band gaps at the HSE06 theoretical level, except for $C_{24}S_{12}$ (4.14 eV energy gap). Moreover, the intrinsic pore sizes of $C_{24}Se_{12}$ are suitable to sieve He from the He/CH_4 mixture, with over 80% separation ratio and nearly 100% selectivity. Our findings not only enlarged the boundary of the 2D family, but also offered another potential method to recover helium from natural gas at ambient conditions.

Received 19th December 2019
Accepted 31st January 2020

DOI: 10.1039/c9ra10696k

rsc.li/rsc-advances

Introduction

Elements of mathematics are widely adopted as the foundation of natural science. In the realm of chemistry, however, geometry owns a non-replaceable position, since all the crystal structures or structural units can find their geometrical analogs.

Inspired by the aesthetics of geometry, chemists and material scientists have long been looking for analogic figures in compounds or crystals. From hexagon to benzene, from truncated icosahedron to fullerene, from honeycomb to graphene, significant breakthroughs in chemistry are tightly connected to those highly symmetric figures. Thus, it has become a competition for scientists to synthesize special morphological materials or design new materials from some attractive patterns.

For example, a Bi_2WO_6 flower nanostructure grown on conductive wire mesh substrates was successfully synthesized as a photocatalyst to improve the separation of photo-generated electron–hole pairs;[1] the large specific surface area (331.3 $m^2 g^{-1}$) and low over-potential of the flower-like FeNi@OCNF nanostructure made it an excellent candidate as a catalyst for the oxygen evolution reaction (OER).[2] Moreover, thistle-shaped nano-composites were found to have high performance as microwave absorbers with broad band features.[3–8] Besides, nanotubes,[9–13] nanowires,[14–17] nanosheets,[18–21] and arrays[22–25] were also fabricated to enlarge the boundary.

With the development of density functional theory (DFT) calculations, efforts have been focused on the prediction of novel structures based on geometric patterns. Though 16 different isohedral convex pentagonal tilings have been discovered so far,[26] less than one third of them are predicted in two-dimensional (2D) materials.[27–31] Among them, perfect band edge position and high carrier mobilities guarantee A_2B (A = P, As, Sb; B = C, Si) family members potential applications in photocatalytic water splitting and 2D devices.[32,33]

Till now, this competition is limited below three dimensions. However, polyhedrons of higher dimensions have been predicted for a long time,[34–36] though they are difficult to imagine. Compared with the stereographic projection to map a sphere into the plane, 4D structures can also be understood in a XYZ system.[37]

Among these fascinating polytopes, the tesseract (or called hypercube) has attracted considerable attention since it is much easier to comprehend, compared to the others. In geometry, it can be regarded as a result of moving a 3D cube one-unit-length into the fourth dimension (Fig. 1 is only the static structure), which contains eight 3D cubes. Although it is impossible to reproduce all the characters of a tesseract in our three-dimensional world, the basic double-shell cubic architecture may be acquired in the molecular level.

A theoretical study about supercubane in 1998 revealed the possibility to polymerize the molecular cubane groups together;[38] later, a DFT investigation on a bonding cubane to create a covalent array in 2006 [39] *via* doping or substitution with donor/acceptor groups further proved the feasibility to expand such cubic frameworks. Based on these results, an O_h-symmetric hypercube structure was predicted by DFT calculations in 2014 (Fig. 1 (b)):[40] the double-shell architectured hypercubane and its perfluorinated analog were proved to be stable, while the removal of the C_8 core yielded a hollow hydrocarbon with a positive electron affinity. Later, the thermal character[41] and substitution effects[42] of the hypercubane,

[a]*Key Laboratory of Marine Chemistry Theory and Technology, Ministry of Education, College of Chemistry and Chemical Engineering, Ocean University of China, Qingdao 266100, China. E-mail: shuweixia@ouc.edu.cn*

[b]*Molecular Nanofabrication Group, MESA+ Institute for Nanotechnology, University of Twente, Enschede, 7522 NB, Netherlands*

† Electronic supplementary information (ESI) available. See DOI: 10.1039/c9ra10696k

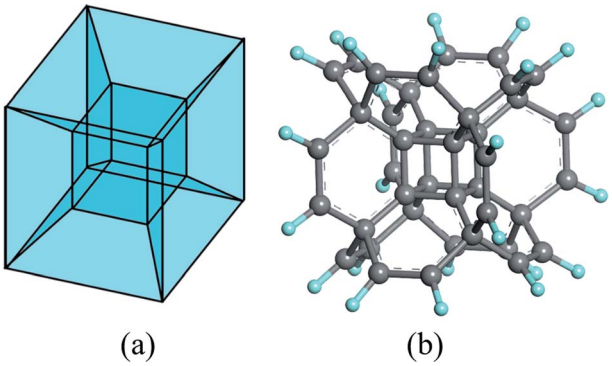

Fig. 1 The structure of (a) tesseract and (b) hypercubane. H and C atoms are colored in cyan and grey.

together with the mechanical properties[43] of its variant, namely hypercubyne, were analyzed, which further demonstrated the stability of the tesseract structure at molecular level.

The successful prediction of hypercubane also encouraged us to explore the tesseract in two dimensional materials. Since the experimental realization of graphene in 2004,[44] the boundary of 2D materials realm extended at an amazing speed, and large numbers of novel nanosheets with atomic thickness were theoretically predicted and synthesized.[45–51] We assume that the combination of attractive 4D polytopes and 2D materials may introduce some fascinating properties and further enlarge their applications.

Herein, by connecting the C_8 core with the bridging VIA group atoms, five stable two-dimensional materials were predicted *via* DFT calculations: except for $C_{24}S_{12}$, other nanosheets exhibit semiconducting characters (E_g = 2.17–3.35 eV). Moreover, the perfect pore size of $C_{24}Se_{12}$ also guarantees its application as an excellent molecular sieve to separate He from He/CH_4. Our predictions not only render a way to access the hypercube structure in two-dimensional world, but also highlight another possibility to recover helium under ambient conditions.

Computation methods

Our computations were performed by VASP (Vienna *ab initio* simulation package),[52] where electron–ion interactions were described *via* projector-augmented plane wave;[53] generalized gradient approximation (GGA)[54] together with Perdew, Burke and Ernzerhof (PBE) were also utilized for the calculations. The DFT-D3 method was adopted for optimal performance.[55]

The energy cutoff was set to 500 eV with 10^{-6} eV as the convergence tolerance for geometry optimizations and electronic property computations; 7 × 7 × 1 and 11 × 11 × 1 Monkhorst–Pack *k*-point meshes were utilized to sample a 2D Brillouin zone for geometry optimizations and band structure calculations, respectively. A 20 Å vacuum layer in the *Z* direction was set to eliminate significant interactions between adjacent layers.

To evaluate their dynamic stabilities, the phonon dispersions of a 3 × 3 × 1 supercell at the PBE level were calculated by CASTEP (Cambridge Sequential Total Energy Package).[56] *Ab initio* molecular dynamics (AIMD) simulations were also performed to verify their thermal stabilities by the VASP code. PBE functional and NVT canonical ensemble[57,58] were used to anneale these 2 × 2 × 1 supercell up to 1500 K for 10 ps with a time step of 1.0 fs.

Since the PBE functional tends to underestimate the band gaps of materials, we recomputed the band structures using the Heyd–Scuseria–Ernzerhof (HSE06)[59] screened-hybrid functional, which has been proved to be a reliable method to predict electronic and optical properties. In the HSE06 hybrid functional, the expression for the exchange-correlation energy is given by:

$$E_{XC}^{HSE} = \frac{1}{4}E_X^{SR}(\mu) + \frac{3}{4}E_X^{PBE,SR}(\mu) + E_X^{PBE,LR}(\mu) + E_C^{PBE} \quad (1)$$

where the short- and long-ranged part of the electron–electron interactions are labeled as SR and LR, respectively; μ represents the screening parameter to define the range-separation and equals to 0.2 in all our calculations.

The possibilities for $C_{24}X_{12}$ as molecular sieve were determined *via* force field molecular dynamic simulations using Forcite code. A 25 Å gas chamber with a 2 × 2 × 1 supercell of $C_{24}X_{12}$ as the roof and graphene as the bottom was constructed, and a 35 Å vacuum layer was set upon $C_{24}X_{12}$ for penetrated gas to freely move. One hundred helium and methane molecules were placed into the chamber before MD simulations. Universal force field[60,61] and NVT ensemble were utilized, and the slab was kept at 300 K, 400 K and 500 K for 2 ns with a time step of 1.0 fs.

Results and discussion

Geometric structures and chemical bonding analysis

To realize the tesseract structure in two-dimension, we started from the dehydrogenated cubane (C_8 core) and choose different bridging atoms to connect the vertices with another. Two factors were considered to select the bridging atoms: (1) the bridging atom should act as a vertex to form a polyhedron coordinated structure; (2) the bridged cubane can only be extended in planar. Thus, atoms with more than three coordination bonds will be sieved out from our list, since atoms with four or more coordination bonds could only be as the centroid rather than a vertex (for example, carbon atoms in methane); and a three-coordinated bridge atom, such as phosphorus, would make it less possible to extend the cubane in the XOY system. Therefore, VIA group atoms became our only choice.

Two different types of nanosheets were constructed following the rule: $C_{24}X_{12}$ and $C_{16}X_{16}$ (X = O, S, and Se) (Fig. 2 and S1†). In $C_{24}X_{12}$, each C_8 shared two bridge chalcogen atoms with an adjacent C_8 core, and six-member rings (C_4X_2, X = O, S, and Se) were expected between the neighboring C_8 units, forming P6/MMM symmetric 2D crystals. The lattice parameters of these monolayers are $a = b$ = 8.85, 9.74 and 10.10 Å, for X = O, S, and Se, respectively. All the $C_{24}X_{12}$ nanosheets are porous structures: two types of crown-like pores, with D_{6h} and D_{3h} symmetries, are formed by three and six C_8s (Table 1); in the *Z* direction, both the pores resulted from the alternating of six-

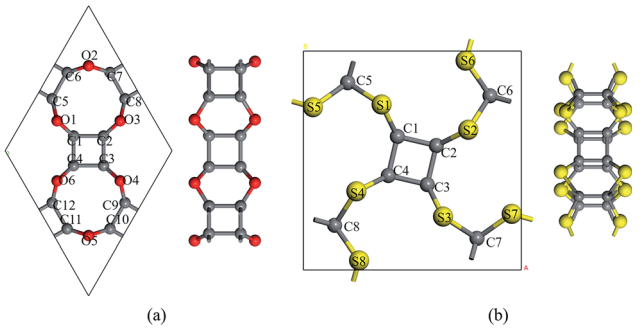

Fig. 2 Snapshots of the optimized structures of (a) $C_{24}O_{12}$ and (b) $C_{16}S_{16}$. Oxygen and sulfur atoms are coloured in red and yellow, respectively.

member rings (C_4X_2) and four-member rings (C_4). Different from the $C_{24}X_{12}$, an eclipsed ethane-like C_2X_6 unit assists the extension of C_8: one pair of overlapping VIA atoms in the Z direction acting as bridging atoms connecting the C_2X_6 unit with the C_8 core; while, the rest two pairs of X atoms are shared by another two adjacent C_2X_6 units, forming $P4/m$ symmetry structures with $a = b = 8.68$ and 9.14 Å for $C_{16}S_{16}$ and $C_{16}Se_{16}$. Three C_2X_6 units are enclosed inside a D_{4h} cage with diameters of 4.49 Å and 4.89 Å for X = S and Se, while surrounded by four C_{2h} 14-member rings with $d = 4.36$ Å and 4.47 Å, respectively (these are the raw diameters of each pore, while results in Table 1 have taken the van der Waals radii of each atom into consideration).

After extending into two-dimension, the C–C bond in the C_8 core is enlarged slightly from 1.57 Å of cubane (Table 1). This is mainly due to the stronger electron-withdrawing ability introduced by the higher electronegativity of oxygen and sulfur atoms. However, the C–C–C bond angle in all these nanosheets remained a perfect 90°, which is inherited from the stability of the cubane.[65,66] Compared to their counterparts of dimethyl compounds, the corresponding C–X bonds shrink a little in $C_{24}X_{12}$, while elongate in $C_{16}X_{16}$, indicating the stronger bonding character of the former with better stability.

Though the bond lengths in $C_{24}X_{12}$ and $C_{16}X_{16}$ exhibited single bond character, electron localization function was also performed for better understanding of their binding nature (Fig. 3 and S2†). High ELF values between the adjacent carbon atoms and C/X atoms demonstrate significant single bond character (Section 2 in Fig. 3); relatively high ELF values around X atoms illustrate the existence of lone-pair electrons. Thus, all the atoms are sp^3 hybridized with only σ bonds expected in these 2D monolayers.

Thermodynamic, dynamic and thermal stabilities

To examine the thermodynamic stability of $C_{24}X_{12}$ and $C_{16}X_{16}$, binding energies (E_b) were first calculated based on the following equation:

$$E_b = (nE_C + mE_X - E_{C_nX_m})/(m + n) \quad (2)$$

where $E_{C/X}$ and $E_{C_nX_m}$ are the total energies of a single atom and tesseract-contained monolayers. According to this definition, a more positive E_b value indicates a more thermodynamically stable structure. $C_{24}X_{12}$ exhibited a much higher binding energy than the majority of the two-dimensional materials (Table 1), such as phosphorene (3.61 eV per atom),[67] silicene (3.94 eV per atom)[68] at the same theoretical level; such high binding energies of the C_nX_m monolayers are reliable evidences for their strong intralayer bonding interactions, which mainly originate from the unusually high decomposition energy of cubane.

The kinetic stabilities of these monolayers were tested by phonon spectra (Fig. 4). No significant soft phonon modes are available in those spectra, demonstrating their excellent kinetic stabilities. Encouragingly, the highest frequencies of these monolayers are over 1000 cm^{-1}, higher than most of the single element and bi-element 2D materials (except graphene (1600 cm^{-1}) and h-BN (1350 cm^{-1})),[69] such as MoS_2 (473 cm^{-1}), WS_2 (~450 cm^{-1}),[70] penta-P_2C (~800 cm^{-1}),[71] and phosphorene (450 cm^{-1}),[72] indicating their robust C–C and C–X bonds.

Moreover, their thermal stabilities were further evaluated *via* AIMD simulations. Three individual MD simulations were performed at the temperatures of 500 K, 1000 K and 1500 K with a 2 × 2 × 1 supercell (Fig. S3 and S4†). The $C_{24}X_{12}$ monolayers do not collapse under 10 ps simulations up to 1000 K, while huge defects emerge in the 14-member-ring for both the $C_{16}S_{16}$ and $C_{16}Se_{16}$ at 1000 K, demonstrating their inferior thermal

Table 1 Structural parameters for $C_{24}X_{12}$ and $C_{16}X_{16}$[a]

	C–C/Å	C–X/Å	C–C–X/° (along XOY direction)	C–C–X/° (along Z direction)	C–X–C/°	Pore size 1/Å	Pore size 2/Å	E_b eV per atom
$C_{24}O_{12}$	1.58	1.39	129.1	121.3	109.2	0.58	3.32	6.18
$C_{24}S_{12}$	1.58	1.77	128.6	125.4	100.0	0.91	3.27	5.71
$C_{24}Se_{12}$	1.57	1.93	127.9	126.9	97.4	0.90	3.20	5.38
$C_{16}S_{16}$	1.59	1.85	130.0	124.5	106.6	0.90	0.71	4.97
$C_{16}Se_{16}$	1.58	2.07	121.4	126.7	102.7	1.01	0.69	4.54
Cubane	1.57	—	—	—	—	—	—	—
CH_3OCH_3	—	1.41	—	—	112.7	—	—	—
CH_3SCH_3	—	1.81	—	—	108.7	—	—	—
CH_3SeCH_3	—	1.94	—	—	110.3	—	—	—

[a] Cubane, methyl ether, dimethylsulfide and methyl selenide were optimized under B3LYP/6-311G+ (d, p) theoretical level[62,63] in Gaussian 09,[64] van der Waals radius of corresponding atoms were taken into consideration to calculate pore sizes.

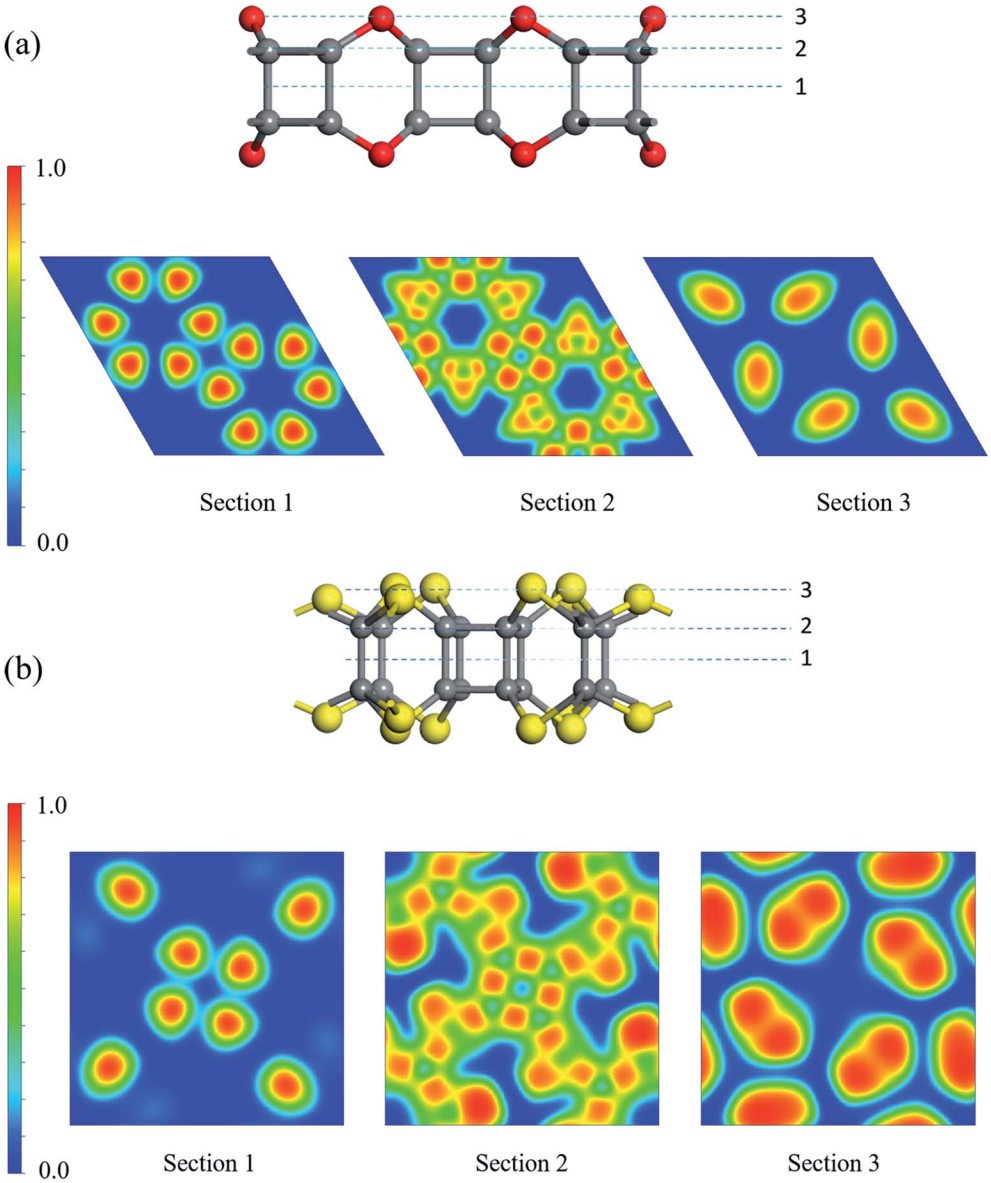

Fig. 3 ELF of (a) $C_{24}O_{12}$ and (b) $C_{16}S_{16}$.

stabilities, and this is also in accordance with the binding energy results. All those reveal that the tesseract containing 2D monolayers have relatively good thermal stabilities and can maintain their structural integrities under ambient conditions.

The above results demonstrate the excellent stabilities of $C_{24}X_{12}$ and $C_{16}X_{16}$, thermodynamically, kinetically and thermally; thus, these nanosheets are possible to be realized experimentally. Therefore, we also proposed several potential approaches to synthesize them (Table 2), expecting their successful experimental synthesis in the near future.

Electronic properties

To investigate their electronic properties, the band structures of $C_{24}X_{12}$ and $C_{16}X_{16}$ were first computed at the GGA/PBE theoretical level (Fig. S5†). All monolayers exhibited semiconducting characters with the $C_{24}Se_{12}$ and $C_{16}S_{16}$ having 2.25 and 1.70 eV indirect bandgaps, respectively, while the rest three nanosheets have 2.27 ($C_{24}O_{12}$), 3.02 eV ($C_{24}S_{12}$) and 1.17 eV ($C_{16}Se_{16}$) direct bandgaps. Both the valence band maximum (VBM) and conduction band minimum (CBM) for $C_{24}O_{12}$, $C_{24}S_{12}$ and $C_{16}Se_{16}$ are located at the Γ point; the VBM for $C_{24}Se_{12}$ is located at the K point, and CBM at Γ point, while the VBM for $C_{16}S_{16}$ is at the Γ point, and the CBM is located at the M point. The analysis of the partial density of states revealed that both the VBM and CBM for $C_{24}X_{12}$ are primarily contributed by the C-2p and X-p orbitals, while the VBMs for $C_{16}X_{16}$ are almost contributed by the X-p orbital, CBM by the C-2p and X-p orbitals.

Since the GGA/PBE method trends to underestimate the bandgap of semiconductors, the Heyd–Scuseria–Ernzerhof

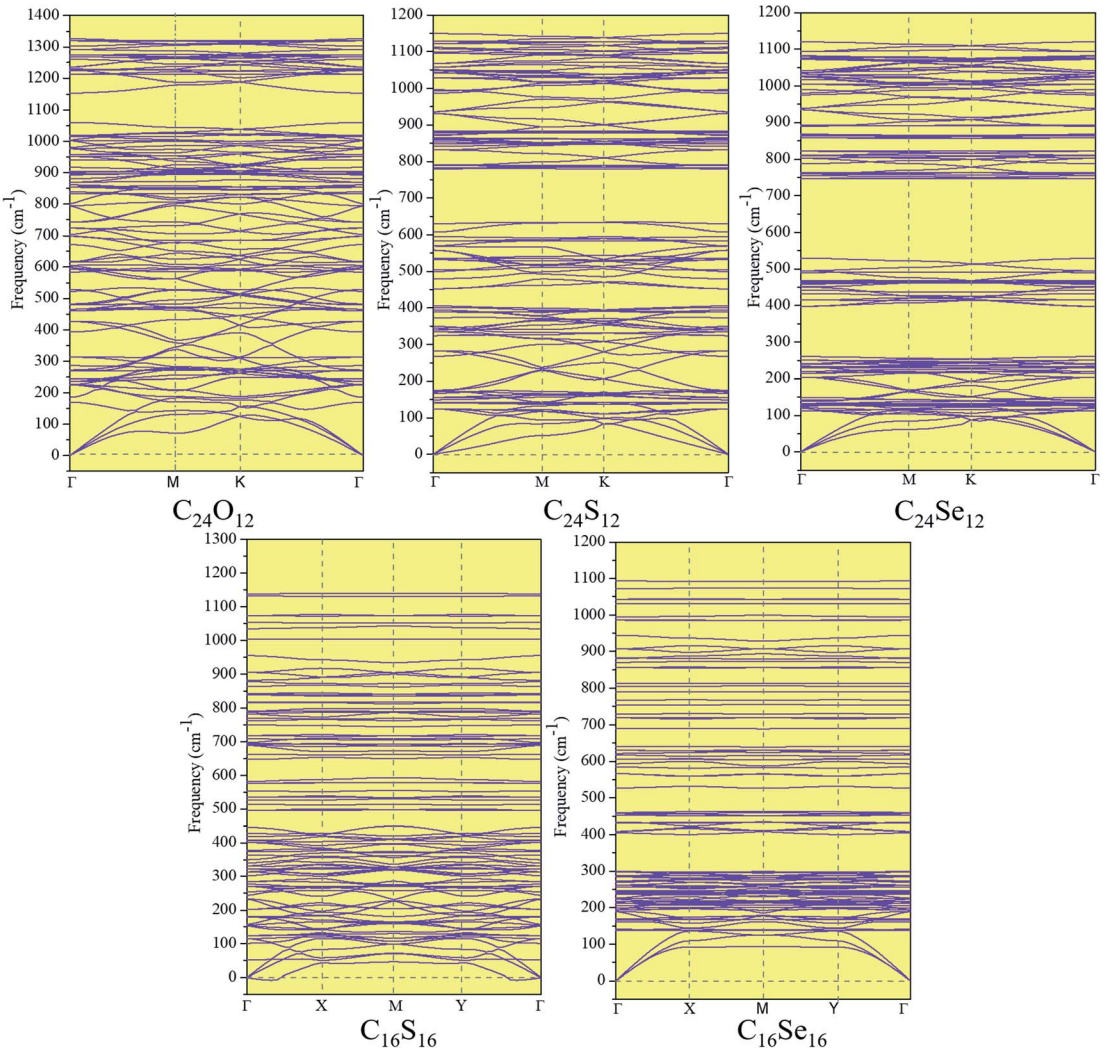

Fig. 4 Phonon band dispersion of C_nX_m, which exhibits high kinetic stability.

Table 2 Possible approaches to experimentally realize $C_{24}X_{12}$ and $C_{16}X_{16}$

Nanosheet	Possible realization approach
$C_{24}O_{12}$	Laser irradiation of cubane under O_2 atmosphere
$C_{24}S_{12}$	Heat cubane with melt sulfur
$C_{16}S_{16}$	Microwave heating the mixture of cubane, S/Se and carbon disulfide or carbon diselenide

(HSE06) hybrid functional is chosen to recalculate the band structure. Compared to GGA, the bandgap of all the five monolayers are enlarged (from 2.17 to 4.14 eV in Fig. 5), while no significant change in the band structures are observed, except for the VBM of $C_{24}Se_{12}$ moved from the *K* point to the middle of the *K* and *Γ* points.

According to the bandgap results under the HSE06 level, the huge gap for $C_{24}X_{12}$ made it less possible to be effective electronic devices; though $C_{16}X_{16}$ have an appropriate bandgap, the fairly flat VBM and CBM will introduce huge effective mass of carriers, also making it unsuitable to be applied as electronic device or photocatalyst. Thus, another path for the application of these monolayers, molecular sieve, was considered.

Molecular sieve

Due to the intrinsic porous structure of $C_{24}X_{12}$ and $C_{16}X_{16}$, their applications as molecular sieve were considered. For $C_{24}X_{12}$, the diameters of the smaller pores are ranged from 3.78 to 4.56 Å; though bigger than the majority of gas molecules, it is impossible for the molecules to pass through considering the electron densities around the pores (Fig. 6(b), 7(b) and S7(b),† iso value = 0.05), similar to the impenetrable nature of graphene.[73–76] Thus, the $C_{16}X_{16}$ nanosheets are also beyond our considerations (Fig. S6†). Therefore, hollow 2 in $C_{24}X_{12}$ becomes the only possible channel.

As one of the most valuable noble gas in the industry, helium is widely applied in the superconductor and space industries;[77]

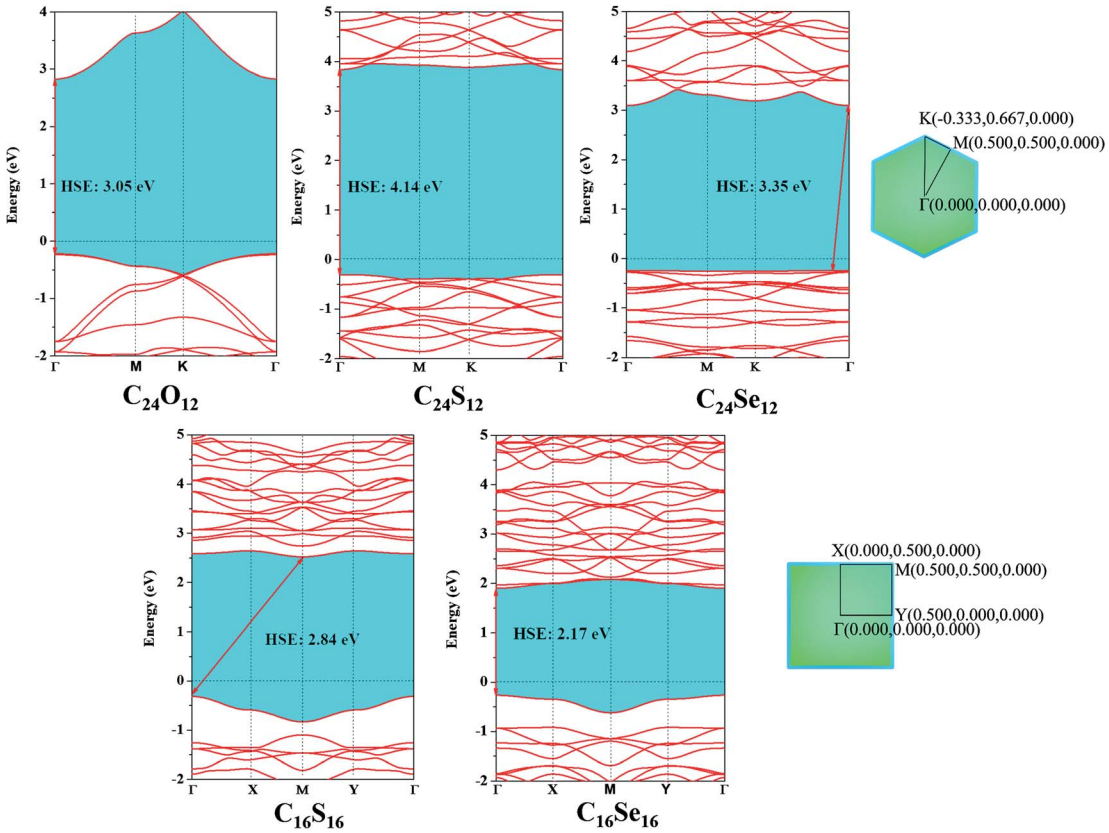

Fig. 5 Band structures of $C_{24}X_{12}$ and $C_{16}X_{16}$ computed by HSE06 and corresponding Brillouin zone path.

He is also a critical resource for future controllable nuclear fusion. Though huge reserves have been prospected on the Moon,[78–83] great challenges and expends still withdraw this inter-planet mining.[84,85] Among its preparation methods available so far, the separation of He from natural gas is one of the best choices;[86] however, such condensation approach is also greatly energy consuming. Thus, different membranes *viz*, polymeric[87] or zeolite[88] frameworks were developed to recover He from the natural gas under ambient conditions, but the toxicity of metal ions and less stability make them less favorable.

The possibilities for $C_{24}X_{12}$ to separate helium from methane were evaluated through energetic barrier and MD simulations. For $C_{24}O_{12}$, the energy barrier for He to penetrate hollow 2 is only 0.6 meV, while that for CH_4 is 79 meV (Fig. S7(c) and (d)†). Though these values are incomparable, such small barriers would make both gas molecules easily pass through the pore. MD simulation results (Fig. S7(e), (f) and S8†) also revealed that it is impossible to separate the He/CH_4 mixture upon $C_{24}O_{12}$.

Different from $C_{24}O_{12}$, the energetic barriers for He to pass the hole of $C_{24}S_{12}$ and $C_{24}Se_{12}$ are 25.9 and 28.1 meV, respectively, while those for CH_4 are 617 and 554 meV (Fig. 6(c), (d), 7(c) and (d)), illustrating that tiny perturbation from the outer system will make He move from one side to another; however, much more energies would be required for CH_4 to penetrate.

Since the possibilities to sieve He from the He/CH_4 mixture were initially verified by energetic barriers, MD simulations were further utilized to evaluate the performance of the separation. The mixture of one hundred He and CH_4 molecules were placed into a 25 Å height chamber 1 composed with $C_{24}X_{12}$ and graphene as its roof and bottom. After 2 ns MD simulations, almost pure helium could be expected in chamber 2 of $C_{24}S_{12}$ and $C_{24}Se_{12}$ under ambient conditions (Fig. S9 and S10†).

The separation ratios of He/CH_4 upon $C_{24}S_{12}$ and $C_{24}Se_{12}$ were analyzed through the distribution of two types of molecules in the slab model (summarized in Table 3). For $C_{24}S_{12}$, the ratio of He in chamber 2 is largely reduced with the rise in temperature, while that for CH_4 increases a little. Compared to that of $C_{24}S_{12}$, the ratio for He in chamber 2 of $C_{24}Se_{12}$ remains almost constant (over 80%) with the increase in temperature and the ratio for CH_4 remains at zero.

Two possible reasons could explain this phenomenon: considering the VDW (van der Waals) radius of sulfur (1.80 Å) and selenium (1.90 Å), the adjusted effective diameters of hollow 2 are 3.27 and 3.20 Å, respectively, for $C_{24}S_{12}$ and $C_{24}Se_{12}$. The bigger pore size of $C_{24}S_{12}$ will make the CH_4 molecules easier to move into the center of the 18-member ring than $C_{24}Se_{12}$. However, the energy for CH_4 to leave the center of $C_{24}S_{12}$ is 382 meV, 13 meV larger than that of $C_{24}Se_{12}$. Thus, though methane molecules can easily get into the cage of both $C_{24}S_{12}$ and $C_{24}Se_{12}$, it is more possible for CH_4 to be trapped inside the hollow 2 of $C_{24}S_{12}$ (verified by more CH_4 molecules in the center of the $C_{24}S_{12}$ holes after MD simulations (Fig. S9 and

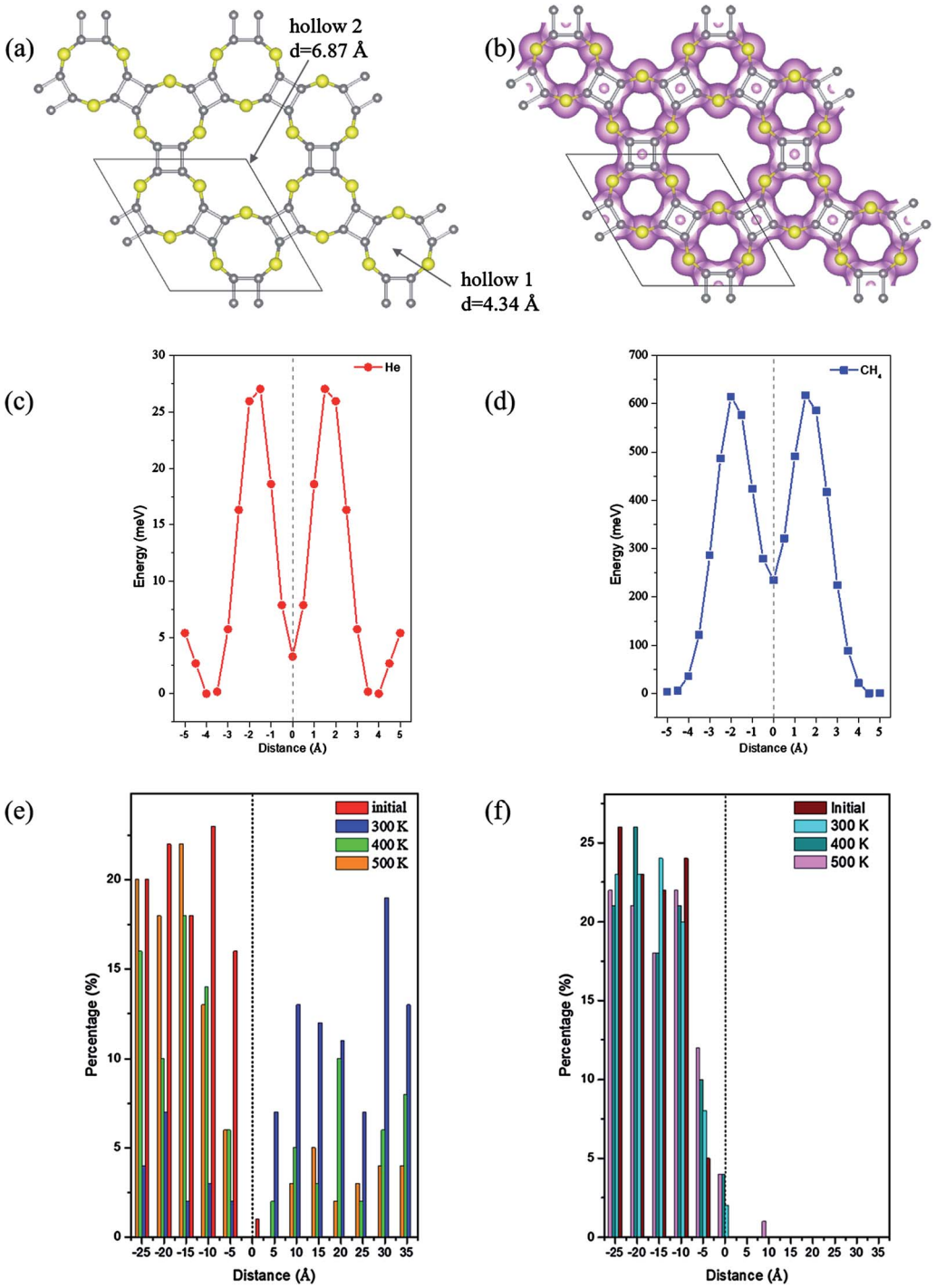

Fig. 6 (a) Structure and (b) electron density of $C_{24}S_{12}$; energetic scan of (c) He and (d) methane pass through hollow 2, the surface of all 18-member-ring centers is set as zero; distribution of (e) He and (f) CH_4 after 2 ns MD simulations at 300 K, 400 K and 500 K.

S10†)), forming a gas-host system. Moreover, the electronegativity of sulfur is bigger than that of selenium; therefore, stronger hydrogen bonds can be expected to stabilize the gas-host system for $C_{24}S_{12}$ than $C_{24}Se_{12}$ after the entrance of methane into the hole (Table S1,† acquired from the optimized structures of $CH_4@C_{24}S_{12}/C_{24}Se_{12}$ in Fig. S11†), leading to the fixation of CH_4 inside the pore rather than leaving or penetration.

Conclusion

We have proposed a series of 2D nanosheets containing the unit of 4D polytope, tesseract, namely $C_{24}X_{12}$ and $C_{16}X_{16}$ (X = O, S and Se). Thermodynamic, kinetic and thermal stabilities were verified by binding energies, phonon dispersion and MD simulations: their excellent stabilities were found to largely

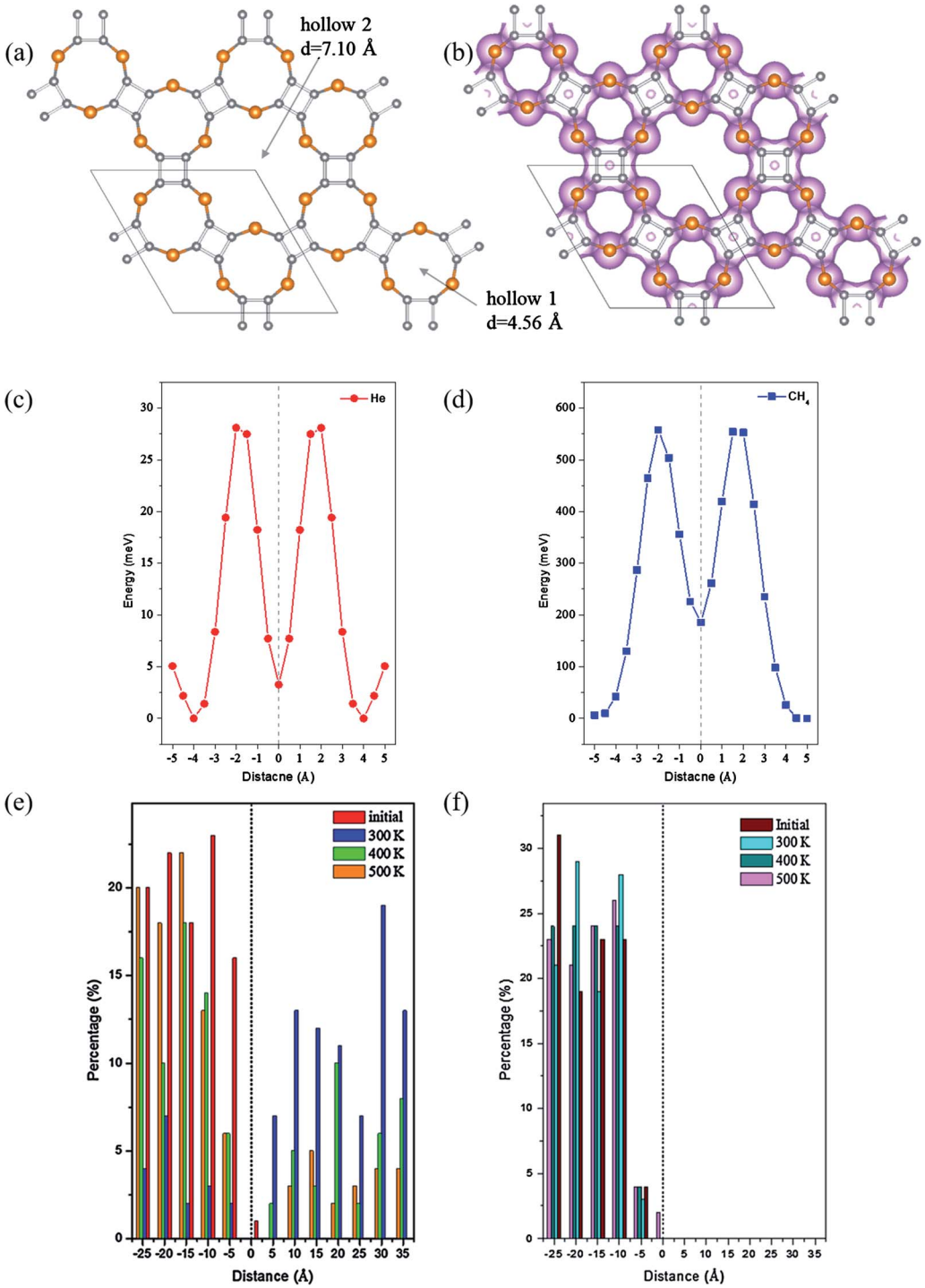

Fig. 7 (a) Structure and (b) electron density of $C_{24}Se_{12}$; energetic scan of (c) He and (d) methane pass through hollow 2; distribution of (e) He and (f) CH_4 after 2 ns MD simulations at 300 K, 400 K and 500 K. Se atom is coloured in orange.

Table 3 Separation ratio of He/CH_4 upon $C_{24}X_{12}$

	$C_{24}O_{12}$		$C_{24}S_{12}$		$C_{24}Se_{12}$	
	He	CH_4	He	CH_4	He	CH_4
300 K	32%	30%	82%	0%	82%	0%
400 K	68%	42%	36%	0%	85%	0%
500 K	66%	50%	21%	1%	84%	0%

originate from the unusual stability of cubane. All these monolayers exhibited semiconducting characters with 2.17 to 3.35 eV bandgaps, except for the insulator nature of $C_{24}S_{12}$ (4.14 eV gap). The fairly flat VBM and CBM make these 2D crystals less probable in the applications of electronic devices and photocatalyst. However, over 80% separation ratio of He from the He/CH_4 mixture upon $C_{24}Se_{12}$ and high selectivity will

make it one of the best candidates as a molecular sieve. This study not only proved the possibility to design novel 2D materials from the prototype of 4D polytopes, extending the realm of the 2D family, but also explored their potential applications. We believe this work would motivate experimental pioneers to realize them in the very near future.

Conflicts of interest

There are no conflicts to declare.

Acknowledgements

The authors would like to acknowledge financial supports from Natural Science Foundation (50673085) and the Ao Shan Talents Cultivation Program Supported by Qingdao National Laboratory for Marine Science and Technology (2017ASTCP-OS02).

References

1 C. Chang, J. Chen, K. Lin, Y. Wei, P. Chao and C. Huang, *J. Alloys Compd.*, 2020, **813**, 152186.
2 P. He, Y. Wu, H. Chen, Z. Zhu, H. Liu, J. Gao and H. Xu, *J. Alloys Compd.*, 2020, **813**, 152192.
3 L. Liu, N. He, T. Wu, P. Hu and G. Tong, *Chem. Eng. J.*, 2019, **355**, 103–108.
4 N. Zhang, Y. Huang, M. Wang, X. Liu and M. Zong, *J. Colloid Interface Sci.*, 2019, **534**, 110–121.
5 J. Ma, X. Wang, W. Cao, C. Han, H. Yang, J. Yuan and M. Cao, *Chem. Eng. J.*, 2018, **339**, 487–498.
6 X. Liu, J. Yu, C. Cui, Y. Sun, X. Li and Z. Li, *J. Phys. D: Appl. Phys.*, 2018, **51**, 265002.
7 J. Deng, S. Li, Y. Zhou, L. Liang, B. Zhao, X. Zhang and R. Zhang, *J. Colloid Interface Sci.*, 2018, **509**, 406–413.
8 N. Wu, C. Liu, D. Xu, J. Liu, W. Liu, Q. Shao and Z. Guo, *ACS Sustainable Chem. Eng.*, 2018, **6**, 12471–12480.
9 J. Xu, L. Gao, J. Cao, W. Wang and Z. Chen, *Electrochim. Acta*, 2010, **56**, 732–736.
10 J. Zou, J. Liu, A. S. Karakoti, A. Kumar, D. Joung, Q. Li, S. I. Khondaker, S. Seal and L. Zhai, *ACS Nano*, 2010, **4**, 7293–7302.
11 B. J. Sanghavi and A. K. Srivastava, *Electrochim. Acta*, 2010, **55**, 8638–8648.
12 P. Kar, S. Zeng, Y. Zhang, E. Vahidzadeh, A. Manuel, R. Kisslinger, K. M. Alam, U. K. Thakur, N. Mahdi, P. Kumar and K. Shankar, *Appl. Catal., B*, 2019, **243**, 522–536.
13 M. Xu, D. N. Futaba, T. Yamada, M. Yumura and K. Hata, *Science*, 2010, **330**, 1364–1368.
14 J. Kim, A. Mirzaei, H. W. Kim and S. S. Kim, *Sens. Actuators, B*, 2019, **285**, 358–367.
15 P. Tan, B. Chen, H. Xu, W. Cai, W. He and M. Ni, *Appl. Catal., B*, 2019, **241**, 104–112.
16 D. Su, Z. Tang, J. Xie, Z. Bian, J. Zhang, D. Yang, D. Zhang, J. Wang, Y. Liu, A. Yuan and Q. Kong, *Appl. Surf. Sci.*, 2019, **469**, 487–494.
17 Z. Wan, D. Lei, W. Yang, C. Liu, K. Shi, X. Hao, L. Shen, W. Lv, B. Li, Q. Yang, F. Kang and Y. He, *Adv. Funct. Mater.*, 2019, **29**, 1805301.
18 Y. Li, X. Lv, J. Lu and J. Li, *J. Phys. Chem. C*, 2010, **114**, 21770–21774.
19 H. Zhao, X. Mu, C. Zheng, S. Liu, Y. Zhu, X. Gao and T. Wu, *J. Hazard. Mater.*, 2019, **366**, 240–249.
20 A. Bafaqeer, M. Tahir and N. A. S. Amin, *Appl. Catal., B*, 2019, **242**, 312–326.
21 R. Li, X. Zhu, Q. Fu, G. Liang, Y. Chen, L. Luo, M. Dong, Q. Shao, C. Lin, R. Wei and Z. Guo, *Chem. Commun.*, 2019, **55**, 2493–2496.
22 X. Li, X. Chen, Z. Yi, Z. Zhou, Y. Tang and Y. Yi, *Micromachines*, 2019, **10**, 164.
23 Y. Lai, J. Huang, H. Zhang, V. Subramaniam, Y. Tang, D. Gong, L. Sundar, L. Sun, Z. Chen and C. Lin, *J. Hazard. Mater.*, 2010, **184**, 855–863.
24 D. Chao, C. R. Zhu, M. Song, P. Liang, X. Zhang, N. H. Tiep, H. Zhao, J. Wang, R. Wang, H. Zhang and H. J. Fan, *Adv. Mater.*, 2018, **30**, 1803181.
25 N. Han, K. R. Yang, Z. Lu, Y. Li, W. Xu, T. Gao, Z. Cai, Y. Zhang, V. S. Batista, W. Liu and X. Sun, *Nat. Commun.*, 2018, **9**, 924.
26 T. Sugimoto, *Graph. Combinator.*, 2015, **31**, 281–298.
27 S. Zhang, J. Zhou, Q. Wang, X. Chen, Y. Kawazoe and P. Jena, *Proc. Natl. Acad. Sci. U. S. A.*, 2015, **112**, 2372–2377.
28 H. L. Zhuang, *Comput. Mater. Sci.*, 2019, **159**, 448–453.
29 J. Li, X. Fan, Y. Wei and G. Chen, *Sci. Rep.*, 2016, **6**, 31840.
30 L. Liu, I. Kankam and H. L. Zhuang, *Comput. Mater. Sci.*, 2018, **154**, 37–40.
31 Z. Liu, H. Wang, J. Sun, R. Sun, Z. F. Wang and J. Yang, *Nanoscale*, 2018, **10**, 16169–16177.
32 S. Sun, F. Meng, Y. Xu, J. He, Y. Ni and H. Wang, *J. Mater. Chem. A*, 2019, **7**, 7791–7799.
33 M. Naseri, S. Lin, J. Jalilian, J. Gu and Z. Chen, *Frontiers of Physics*, 2018, **13**, 138102.
34 H. S. M. Coxeter, *Proc. Lond. Math. Soc.*, 1938, **2–43**, 33.
35 R. V. B. Rucker, *Geometry, Relativity, and the Fourth Dimension*, Dover Pubns, 1977.
36 E. H. Neville, *The Fourth Dimension*, Merchant Books, 2007.
37 W. Armstrong and R. Burton, in *Stereoscopic Displays & Applications*, International Society for Optics and Photonics, 1990.
38 B. Winkler and V. Milman, *Chem. Phys. Lett.*, 1998, **293**, 284–288.
39 B. Herrera, F. Valencia, A. H. Romero, M. Kiwi, R. Ramírez and A. Toro-Labbé, *J. Mol. Struct.*, 2006, **769**, 183–187.
40 F. Pichierri, *Chem. Phys. Lett.*, 2014, **612**, 198–202.
41 M. M. Maslov and K. P. Katin, *Chem. Phys. Lett.*, 2016, **644**, 280–283.
42 F. Pichierri, *Theor. Chem. Acc.*, 2017, **136**, 114.
43 S. W. Cranford, *Extreme Mechanics Letters*, 2018, **22**, 19–26.
44 K. S. Novoselov, A. K. Geim, S. V. Morozov, D. Jiang, Y. Zhang, S. V. Dubonos, I. V. Grigorieva and A. A. Firsov, *Science*, 2004, **306**, 666–669.
45 M. Kawaguchi, S. Kuroda and Y. Muramatsu, *J. Phys. Chem. Solids*, 2008, **69**, 1171–1178.

46 H. Liu, A. T. Neal, Z. Zhu, Z. Luo, X. Xu, D. Tomanek and P. D. Ye, *ACS Nano*, 2014, **8**, 4033–4041.
47 B. Aufray, A. Kara, S. Vizzini, H. Oughaddou, C. Leandri, B. Ealet and G. Le Lay, *Appl. Phys. Lett.*, 2010, **96**, 183102.
48 R. S. Sundaram, M. Engel, A. Lombardo, R. Krupke, A. C. Ferrari, P. Avouris and M. Steiner, *Nano Lett.*, 2013, **13**, 1416–1421.
49 B. Radisavljevic, A. Radenovic, J. Brivio, V. Giacometti and A. Kis, *Nat. Nanotechnol.*, 2011, **6**, 147–150.
50 M. Naguib, V. N. Mochalin, M. W. Barsoum and Y. Gogotsi, *Adv. Mater.*, 2014, **26**, 992–1005.
51 M. Naguib, M. Kurtoglu, V. Presser, J. Lu, J. Niu, M. Heon, L. Hultman, Y. Gogotsi and M. W. Barsoum, *Adv. Mater.*, 2011, **23**, 4248–4253.
52 G. Kresse and J. Furthmüller, *Comput. Mater. Sci.*, 1996, **6**, 15–50.
53 P. E. Blöchl, *Phys. Rev. B: Condens. Matter Mater. Phys.*, 1994, **50**, 17953–17979.
54 J. P. Perdew, K. Burke and M. Ernzerhof, *Phys. Rev. Lett.*, 1996, **77**, 3865–3868.
55 S. Grimme, J. Antony, S. Ehrlich and H. Krieg, *J. Chem. Phys.*, 2010, **132**, 154104.
56 S. J. Clark, M. D. Segall, C. J. Pickard, P. J. Hasnip, M. J. Probert, K. Refson and M. C. Payne, *Z. Kristallogr.*, 2005, **220**, 567–570.
57 S. Nosé, *Mol. Phys.*, 1984, **52**, 255–268.
58 B. Leimkuhler, E. Noorizadeh and F. Theil, *J. Stat. Phys.*, 2009, **135**, 261–277.
59 J. Heyd, G. E. Scuseria and M. Ernzerhof, *J. Chem. Phys.*, 2003, **118**, 8207–8215.
60 A. K. Rappe, K. S. Colwell and C. J. Casewit, *Inorg. Chem.*, 1993, **32**, 3438–3450.
61 A. K. Rappe, C. J. Casewit, K. S. Colwell, W. A. Goddard and W. M. Skiff, *J. Am. Chem. Soc.*, 1992, **114**, 10024–10035.
62 A. D. McLean and G. S. Chandler, *J. Chem. Phys.*, 1980, **72**, 5639–5648.
63 R. C. Binning and L. A. Curtiss, *J. Comput. Chem.*, 1990, **11**, 1206–1216.
64 M. J. Frisch, G. W. Trucks, H. R. Fukuda, J. Hasegawa, M. Ishida, T. Nakajima, Y. Honda, O. Kitao, H. Nakai, T. Vreven, J. A. Montgomery Jr, J. E. Peralta, F. Ogliaro, M. Bearpark, J. J. Heyd, E. Brothers, K. N. Kudin, V. N. Staroverov, R. Kobayashi, J. Normand, K. Raghavachari, A. Rendell, J. C. Burant, S. S. Iyengar, J. Tomasi, M. Cossi, N. Rega, J. M. Millam, M. Klene, J. E. Knox, J. B. Cross, V. Bakken, C. Adamo, J. Jaramillo, R. Gomperts, R. E. Stratmann, O. Yazyev, A. J. Austin, R. Cammi, C. Pomelli, J. W. Ochterski, R. L. Martin, K. Morokuma, V. G. Zakrzewski, G. A. Voth, P. Salvador, J. J. Dannenberg, S. Dapprich, A. D. Daniels, O. Farkas, J. B. Foresman, J. V. Ortiz, J. Cioslowski and D. J. Fox, Gaussian, Inc., Wallingford, CT, 2009.
65 P. E. Eaton, *Angew. Chem., Int. Ed. Engl.*, 1992, **31**, 1421–1436.
66 K. F. Biegasiewicz, J. R. Griffiths, G. P. Savage, J. Tsanaktsidis and R. Priefer, *Chem. Rev.*, 2015, **115**, 6719–6745.
67 L. Li, Y. Yu, G. J. Ye, Q. Ge, X. Ou, H. Wu, D. Feng, X. H. Chen and Y. Zhang, *Nat. Nanotechnol.*, 2014, **9**, 372–377.
68 L. Huang, P. Gong and Z. Zeng, *Phys. Rev. B: Condens. Matter Mater. Phys.*, 2015, **91**, 205433.
69 H. Şahin, S. Cahangirov, M. Topsakal, E. Bekaroglu, E. Akturk, R. T. Senger and S. Ciraci, *Phys. Rev. B: Condens. Matter Mater. Phys.*, 2009, **80**, 155453.
70 A. Molina-Sanchez and L. Wirtz, *Phys. Rev. B: Condens. Matter Mater. Phys.*, 2011, **84**, 155413.
71 M. Naseri, S. Lin, J. Jalilian, J. Gu and Z. Chen, *Frontiers of Physics*, 2018, **13**, 138102.
72 G. Qin, Q. Yan, Z. Qin, S. Yue, M. Hu and G. Su, *Phys. Chem. Chem. Phys.*, 2015, **17**, 4854–4858.
73 Y. Zhao, Y. Xie, Y. Y. Hui, L. Tang, W. Jie, Y. Jiang, L. Xu, S. P. Lau and Y. Chai, *J. Mater. Chem. C*, 2013, **1**, 4956.
74 R. R. Nair, H. A. Wu, P. N. Jayaram, I. V. Grigorieva and A. K. Geim, *Science*, 2012, **335**, 442–444.
75 J. S. Bunch, S. S. Verbridge, J. S. Alden, A. M. van der Zande, J. M. Parpia, H. G. Craighead and P. L. McEuen, *Nano Lett.*, 2008, **8**, 2458–2462.
76 X. Zheng, M. Zhang, X. Shi, G. Wang, L. Zheng, Y. Yu, A. Huang, P. K. Chu, H. Gao, W. Ren, Z. Di and X. Wang, *Adv. Funct. Mater.*, 2015, **25**, 1805–1813.
77 F. G. Kerry, *Industrial Gas Handbook: Gas Separation and Purification*, 2007.
78 G. I. Dimov, *J. Fusion Energy*, 2014, **33**, 453–455.
79 F. H. Cocks, *Icarus*, 2010, **206**, 778–779.
80 D. Li, H. Liu, W. Zhang, Y. Li and C. Xu, *Sci. China: Earth Sci.*, 2010, **53**, 1103–1114.
81 Z. Wang, Y. Li, J. Jiang and D. Li, *Sci. China: Earth Sci.*, 2010, **53**, 1365–1378.
82 W. Fa and Y. Jin, *Icarus*, 2007, **190**, 15–23.
83 J. R. Johnson, T. D. Swindle and P. G. Lucey, *Geophys. Res. Lett.*, 1999, **26**, 385–388.
84 J. C. Woods, *J. Appl. Physiol.*, 2013, **114**, 705–706.
85 U. Guven and P. Kuchhal, *Appl. Mech. Mater.*, 2011, **110–116**, 2054–2061.
86 S. Faramawy, T. Zaki and A. A. E. Sakr, *J. Nat. Gas Sci. Eng.*, 2016, **34**, 34–54.
87 C. Zhang, R. P. Lively, K. Zhang, J. R. Johnson, O. Karvan and W. J. Koros, *J. Phys. Chem. Lett.*, 2012, **3**, 2130–2134.
88 C. A. Scholes, G. W. Stevens and S. E. Kentish, *Fuel*, 2012, **96**, 15–28.